Temperature dependence of electronic conductivity from *ab initio* thermal simulation

R. Hussein[a], C. Ugwumadu[b], K. Nepal[a], R. M. Tutchton[b], K. Kappagantula[c], D. A. Drabold[a]

[a]*Department of Physics and Astronomy, Nanoscale and Quantum Phenomena Institute (NQPI), Ohio University, Athens, 45701, OH, USA*
[b]*Quantum and Condensed Matter Physics (T-4) Group, Los Alamos National Laboratory, Los Alamos, 87545, NM, USA*
[c]*Pacific Northwest National Laboratory, Richland, 99354, WA, USA*

Abstract

We present a temperature-dependent extension of the approximate electronic conductivity formula of Hindley and Mott that leverages time-averaged fluctuations of the electronic density of states obtained from *ab initio* molecular dynamics. By thermally averaging the square of the density of states near the Fermi level, we obtain an estimate of the temperature dependence of the conductivity. This approach—termed the thermally-averaged Hindley-Mott (TAHM) method—was applied to five representative systems: crystalline aluminum (c-Al), aluminum with a grain boundary (Al_{GB}), a four-layer graphene–aluminum composite (Al–Gr), amorphous silicon (a-Si) and amorphous germanium–antimony–telluride (a-GST). The method reproduces the expected Bloch–Grüneisen decrease in conductivity for c-Al and Al_{GB}. Generally, the reduction (increase) in conductivity for metallic (semiconducting) materials are reproduced. It captures microstructure-induced, thermally activated conduction in multilayer Al–Gr, a-Si and a-GST. Overall, the approach provides a computationally efficient link between time-dependent electronic structure and temperature-dependent transport, offering a simple and approximate tool for exploring electronic conductivity trends in complex and disordered materials.

Keywords: fluctuating; fermi level; thermal; TAHM; Mott's conductivity; electronic density of states

1. Introduction

The electrical conductivity of condensed matter is a dynamical property that emerges from charge carriers moving through a time-dependent landscape influenced by lattice vibrations, defects, electronic scattering disorder, and external fields. Capturing that interplay—electrons responding to ionic motion on femto- to pico-second scales while also scattering from static inhomogeneities—is essential for predicting material performance and interpreting transport experiments across metals, semiconductors, and disordered materials.

Two main approaches are used to compute electronic conductivity. The first is the semiclassical Boltzmann framework, in which charge carriers are treated as quasiparticles whose distribution obeys the Boltzmann transport equation (BTE). In the weak-field, near-equilibrium limit, the linearized BTE with a relaxation-time approximation (RTA) [1, 2] yields a conductivity tensor and underpins most transport calculations in metals and semiconductors [3, 4], as implemented in BOLTZ-TRAP [5, 6] and EPW [7]. Iterative solutions beyond the RTA can treat inelastic and anisotropic scattering more accurately [8], but the semiclassical picture still assumes coherent band transport and breaks down under strong disorder, localization, or ultrafast excitation.

When such effects become significant, fully quantum linear-response formulations are preferred. Within the quantum picture, conductivity may be obtained from linear response (Kubo) [9], its fluctuation–dissipation counterpart (Green–Kubo) [10, 11, 12], or the single-electron eigenstate formulation known as the Kubo–Greenwood formula (KGF), widely used with density functional theory (DFT) [13, 14, 15, 16, 17, 18].

Mott writes the KGF for the conductivity as [19, 20]:

$$\sigma \sim \frac{2\pi e^2 \hbar^3}{m^2} \left| D(E_f) \right|^2_{\text{avg}} N^2(E_F) \tag{1}$$

where

$$D(E_f) = \int \psi_{l'}^* \frac{\partial}{\partial x} \psi_l d^3 x \tag{2}$$

for single-particle states ψ and "avg" indicates an average over a small window near the Fermi level (E_f). $N(E_f)$ is the density of states at the Fermi level, and σ is the DC conductivity. From a Fermi Golden Rule argument it is natural to interpret electronic conduction in terms of quantum transitions at the Fermi level. Thus, $\sigma \propto N^2(E_F)$. Hindley reached a similar conclusion by invoking a random phase approximation [21]. We introduced what we call the "N^2 method" based upon this proportionality to obtain a positive additive distribution that provides information about the local intensity of electrical conductivity and applied it to a copper-carbon composite material [22], as well as defective tungsten [23]. All these were obtained for the case of a static lattice. While one intuitively thinks of the electronic density of states (EDOS) at the Fermi level as a rough measure of conductivity, in fact it is the *squared* EDOS.

The primary innovation of this paper is to exploit the $\sigma \propto N^2(E_F)$ approach by approximately including the effects of

atomic motion – estimating the temperature dependence of the electrical conductivity which is in general a challenging task. Abtew *et al* [24] and Subedi *et al* [25] showed that averaging the KGF over a suitably equilibrated *ab initio* MD simulation (at constant temperature T) provides useful estimates for the T dependence of σ, suggesting the possible utility of averaging N^2 in a similar way by estimating the temperature dependent conductivity as:

$$\sigma(T) \propto \frac{1}{n} \sum_{i=1}^{n} N^2(E_f, t_i) \tag{3}$$

in which i indexes a time step and the number of times steps n is assumed to be large enough that the quantity $\sigma(T)$ is converged. In this paper, we showed that equation 3 provides useful estimates of temperature-dependence and determine suitable runtimes, "n", post equilibration to obtain $\sigma(T)$.

This approach is inherently approximate. Its main assumptions are: (1) an adiabatic treatment in which transport is estimated by averaging over "Born–Oppenheimer" snapshots; (2) classical dynamics, which neglects lattice quantization (phonons); (3) interpretation of the Kohn–Sham (KS) eigenvalues as a proxy for the electronic density of states at the Fermi level; (4) omission of any time-step dependence in the matrix element $D(E_f)$; and (5) applicability primarily to homogeneous systems—while the full Kubo–Greenwood formula yields a complete conductivity tensor, that tensor information is not retained in the present simplification. A practical advantage is that $N^2(E_f)$ can be extracted as a byproduct of quantum MD, making the workflow straightforward to implement.

In what follows, we show that this simple scheme, which we name the thermally averaged Hindley-Mott (TAHM) method, produces temperature trends for the conductivity comparable to those obtained from the more rigorous KGF method [25] and from experiment [26]. Both the metallic reduction in conductivity with increasing temperature and semiconducting increase with increasing temperature is reproduced. As first seen by Subedi *et al.* [25], the scheme produces reasonable results in a metal (Al) even for temperatures well below the Debye temperature, which is surprising for a classical simulation.

We also report a microstructure-dependent semiconducting behavior in aluminum–graphene composite with 4 layers of AB-stacked graphene featuring undulating (worm-like) morphology [27, 28, 29]. Furthermore, we compare our results for amorphous silicon with KGF-based conductivity data [24] as well as experimental conductivity data [30, 31, 32], and extend the analysis to the phase-change memory material, amorphous germanium–antimony–telluride [33].

2. Methods

2.1. Structural Models

Five materials of interest are considered in this study: crystalline aluminum (c-Al), aluminum with a grain boundary (Al_{GB}), aluminum–graphene composites (Al–Gr), amorphous silicon (a-Si), amorphous germanium–antimony–telluride,
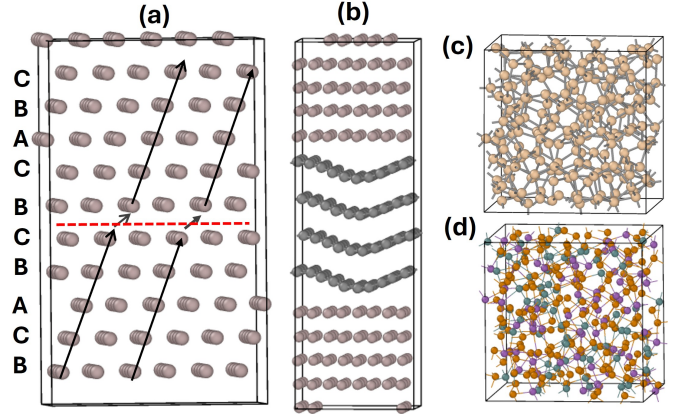

Figure 1: Structural representation of (a) aluminum with grain boundary (AB stacking fault represented by the red dashed line), (b) aluminum-graphene composite formed with the worm-like 4-layer (AB-stacked) graphene (gray), (c) amorphous silicon, and (d) amorphous germanium (teal)-antimony (purple)-telluride (brown) .

$Ge_2Sb_2Te_5$ (a-GST). The Vienna *Ab-initio* Simulation Package (VASP) [34] was used for all simulations.

The c-Al model is a face-centered cubic (FCC) cubic containing 256 atoms (see Figure S1e). This configuration is used for the bulk regions of the Al_{GB} structure, while the grain-boundary region contains a stacking fault (red dashed line in Figure 1a). Similarly, the same c-Al configuration is used for the Al–Gr composite structure, in which the graphene region is a four-layer (AB-stacked) undulating ("worm-like") sheet (Figure 1b).

The undulating worm-like graphene morphology results from conjugate-gradient (CG) energy relaxation of the Al–Gr structure, starting from initially flat graphene layers between the Al slabs with an interfacial Al–C distance of 3.22 Å. This configuration may mimic high-stress metastable interfaces produced by solid phase processing used to fabricate AA1100 alloys reinforced with reduced-graphene-oxide nanoparticles, yielding ultra-conductive Al composites [35, 36].

For a-Si, we employed the 216-atom model of Djordjević, Thorpe, and Wooten [37], generated using the Wooten–Winer–Weaire approach [38] and previously analyzed in other studies [39, 40] (Figure 1c). The 315-atom a-GST model (Figure 1d) was taken from Reference [33] .

2.2. Implementation

The electronic density of states for all systems was computed using VASP [34] with projector augmented-wave (PAW) potentials [41], the Perdew–Burke–Ernzerhof (PBE) exchange–correlation functional [42], and a Gaussian smearing width of 0.01 eV. For the time-dependent analysis, snapshots were extracted from *ab initio* molecular dynamics (AIMD) simulations performed at different temperatures, maintained by a Nosé–Hoover thermostat [43].

The AIMD trajectories spanned several picoseconds, with integration time steps of 0.5, 1.0, 0.75, 1.0, and 2.0 fs for c-Al (2.5 ps), Al_{GB} (5 ps), Al–Gr (3 ps), a-Si (4 ps), and a-GST (7.5-10 ps), respectively. This framework is general and can equally

incorporate electronic structures sampled from longer MD simulations based on classical, empirical, or machine-learning interatomic potentials. The Γ-point was used to sample the Brillouin zone for all simulations, with periodic boundary conditions. The cutoff energy for a-GST was 320 eV and 400 eV was employed for the other structures. The selected simulation times were chosen to ensure convergence of the averaging at the Fermi level.

The instantaneous electronic density of states (EDOS) at time t_μ, (obtained from a constant temperature MD simulation), is:

$$D(E, t_\mu) = \sum_i \delta(E - \epsilon_i(t_\mu)) \tag{4}$$

and $\epsilon_i(t_\mu)$ is a Kohn–Sham eigenvalue at time step t_μ.

The Kohn-Sham states relevant to the DC conductivity are those near the Fermi level E_f. We therefore define the instantaneous N^2 at time t as:

$$N^2(E_f, T; t) = \left[\int D(E, T, t)\, \delta_h(E - E_f)\, dE \right]^2$$
$$= \left[\sum_i \delta_h(\epsilon_i(t) - E_f(t)) \right]^2 \tag{5}$$

$$\delta_h(\varepsilon) = \frac{1}{\sqrt{2\pi}\, h} \exp\left(-\frac{\varepsilon^2}{2h^2} \right) \tag{6}$$

where we take δ_h to be a Gaussian of width h. The value of h is tuned to the presence (or absence) of an electronic gap: $h = 0.35$ eV for c-Al and Al_{GB}, 0.2 eV for Al–Gr, 0.7 eV for a-Si, and 0.54 eV for a-GST. These values are larger than the mean spacing between KS eigenvalues at E_f, so that h is broad enough to capture thermal fluctuations of near-E_f states while remaining narrow enough to resolve intrinsic spectral features.[1] At each time step, the Fermi level is shifted so that $E_f = 0$ for reference.

The next step is to estimate $\sigma(T)$ by averaging over a converged trajectory of a well-equilibrated atomic configuration at temperature T (see Equation 3). We sample the Born–Oppenheimer (BO) trajectory using a running (cummulative) time average over post-equilibration time steps $\{t_k\}_{k=1}^K$. Using Equations 1–6, we compute TAHM ($\langle N^2 \rangle_t$) as:

$$\langle N^2 \rangle_t = \frac{1}{K} \sum_{k=1}^K N^2(E_f, T; t_k) \tag{7}$$

This yields an estimate of $\sigma(T)$ once fluctuations becomes small for a sufficiently long simulation.

2.3. Estimating Conductivity from $\langle N^2 \rangle_t$

The temperature dependence of the electronic conductivity can be estimated by correlating $\langle N^2 \rangle_t$ with experimental conductivity data at a known temperature. Fitting a single data point of $\langle N^2 \rangle_t$ to a corresponding experimental conductivity

_____

[1] For small systems or when few states lie near E_f, this broadening choice becomes more delicate.

provides an estimate of the proportionality constant associated with the conductivity matrix element [22].

For example, the Al–Gr composite structure exhibits an experimentally measured conductivity of $\sigma_{\text{Al–Gr}} \approx 3.87 \times 10^7$ S/m at 300 K [44]. We first define a single calibration factor η at $T_0 = 300$ K from the measured conductivity of Al–Gr:

$$\eta = \left. \frac{\sigma_{\text{Al–Gr}}(T_0)}{\langle N^2 \rangle_t^{\text{Al–Gr}}(T_0)} \right|_{T_0 = 300 \text{ K}} \tag{8}$$

We then use this proportionality to map the TAHM of each system onto a predicted conductivity and resistivity at any temperature:

$$\sigma_{\text{N}^2}(T) = \eta\, \langle N^2(T) \rangle_t\,; \qquad \rho_{\text{N}^2}(T) = \frac{1}{\eta\, \langle N^2(T) \rangle_t} \tag{9}$$

hence giving a quantitative estimate of temperature-dependent electronic transport behavior.

3. Results and Discussion

For brevity, we will denote $N^2(E_f, T, t)$ in Equation 5 by N_t^2. The character of temperature-induced EDOS fluctuations around the Fermi level differs among the materials. The instantaneous EDOS at selected time steps and temperatures for all structures is shown in Figure 2a–e, and all similar plots for all temperatures considered per structure is shown in Figure S2a–e. Except for a-Si, which was analyzed over the broader range of 200–1800 K, the temperature range for the other systems extends up to 700 K. For clarity, the Fermi level in each plot has been shifted to zero (indicated by the dashed black line).

Appreciable temperature-dependent fluctuations near E_F are observed for c-Al, Al_{GB}, and Al–Gr (Figure 2a–c). The fluctuations are most pronounced for a-Si (Figure 2d), where the electronic gap broadens with increasing temperature and simulation time. They are less pronounced for a-GST (Figure 2e). The following subsections present a detailed analysis for each system.

3.1. Aluminum: Crystalline and Grain Boundary Structures

The analysis for the c-Al and Al_{GB} systems were performed over a temperature range of 50–700 K. The characteristic electronic density of states (EDOS) profile of aluminum is largely preserved, exhibiting extended near-E_f states, in both c-Al (Figure 3a,b) and Al_{GB} (Figure S3a,b). Early MD steps that exhibit strong non-equilibrium fluctuations before thermal stabilization were not included in the analysis. For c-Al (Al_{GB}), this included the first 0.8 ps (2 ps). The running average implementation on N_t^2 effectively smoothened these oscillations to yield convergence as shown in Figure 3b and S3b for c-Al and Al_{GB}, respectively. The time-averaged $\langle N^2 \rangle_t$ were determined once the running average varied by less than 5% over successive steps and exhibit a decrease from 100 K to 700 K in both c-Al (Figure 3c) and Al_{GB} (Figure 3d).

Next, we compare $\langle N^2 \rangle_t$ results with experiment in Figure 3e. The experimentally measured resistivity from Reference [26]
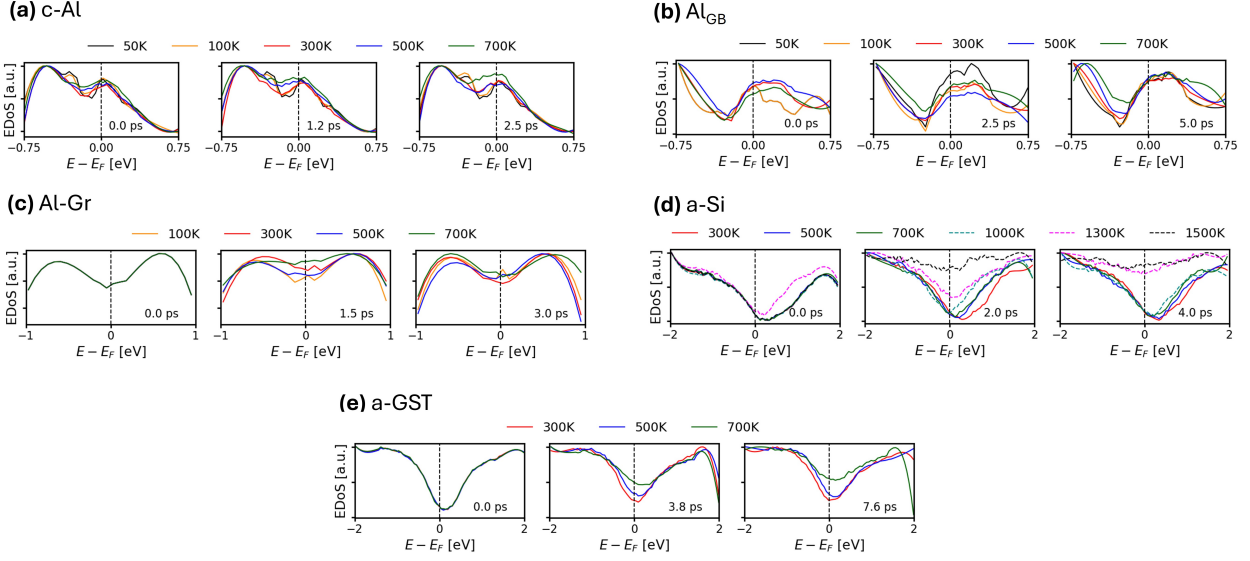
Figure 2: The electronic density of states near the Fermi level obtained from the MD simulations at different instantaneous Born-Oppenheimer snapshots, showing for (a) Crystalline aluminum, (b) Aluminum with a grain boundary, (c) Aluminum-graphene composite, (d) amorphous silicon, and relaxed (e) amorphous germanium–antimony–telluride.

(up to 300 K) is plotted against the resistivity inferred from the $\langle N^2 \rangle_t$ using Equation 9. To convert $\langle N^2 \rangle_t$ into a conductivity estimate, we choose a reference temperature $T_0 = 50$ K and determine a proportionality constant η to be $\approx 2.5 \times 10^{-2}$. This choice is consistent with the KGF analysis of Subedi *et al.* [25], where they also adopt $T_0 = 50$ K for the same dataset. For crystalline aluminum, electron–phonon scattering follows the Bloch–Grüneisen (BG) behavior which suggests that in the low-T regime ($T \ll \Theta_D$) the phonon contribution scales steeply ($\propto T^5$) and becomes small compared to the defect-induced residual resistivity [45].

For c-Al in Figure 3e, the temperature dependence predicted by $\langle N^2 \rangle_t$ is consistent with the KGF analysis [25] and agrees qualitatively with both the experimental data and the extrapolated BG fit. The resistivity of Al_{GB} is higher than that of c-Al and shows a larger deviation from experiment, especially at high temperature, as expected due to the additional grain-boundary scattering. Nevertheless, at lower temperatures its resistivity remains close to c-Al and to the experimental curve, and the overall trend with T is preserved, as seen more clearly in Figure 3f. Between 100 and 700 K, crystalline Al shows a $\sim 9.53\%$ reduction in conductivity, compared to $\sim 11.73\%$ for Al_{GB}. This behavior parallels the SPC-based results of Reference [25], where local conductivity is reduced at Al grain boundaries.

3.2. Aluminum–Graphene Composite

The running time average of N_t^2 for Al–Gr converges well and increases smoothly with temperature over the range 100–700 K (Figure 4a). Instantaneous N_t^2 traces at the simulated temperatures are shown in Figure S4. After calibrating the conductivity at a reference temperature of 300 K (Section 2.3), $\sigma_{N^2}(T)$ exhibits an approximately linear increase with temperature, with slope 1.49×10^4 S m^{-1} K^{-1} (Figure 4b). Within a
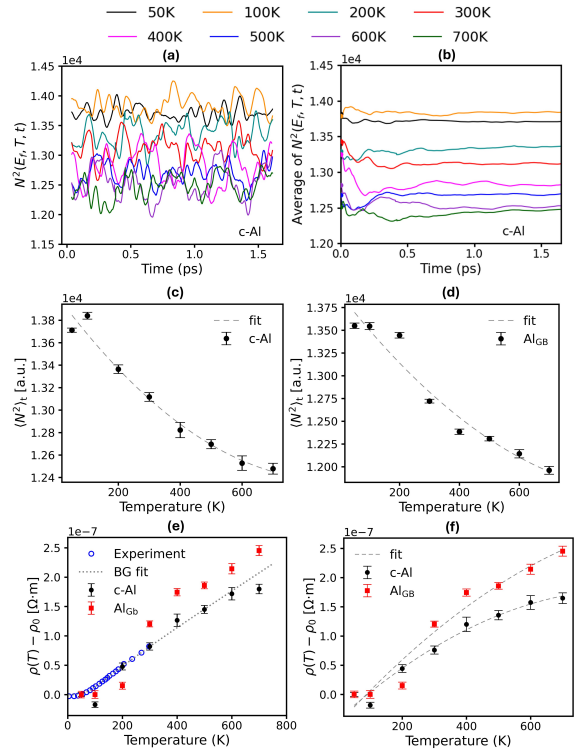

Figure 3: Analysis for crystalline aluminum (c-Al) and aluminum with a grain boundary (Al_{GB}). (a) Instantaneous N_t^2 from the EDOS at different temperatures and (b) the convergence of the running time-average of N_t^2 for c-Al (similar plots for Al_{GB} are provided in Figure S3a and b). Converged $\langle N^2 \rangle_t$ versus temperature with quadratic fit for (c) c-Al and (d) Al_{GB}. (e) Experimental resistivity [26] compared with values from $N^2(E_F)$ for c-Al and Al_{GB}; Bloch–Grüneisen (BG) predictions are included. (f) Temperature-dependent resistivity for c-Al and Al_{GB}; from $\langle N^2 \rangle_t$, with error bars from MD time averaging.
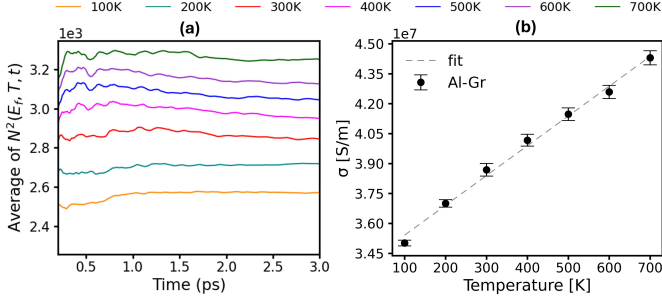
4

Figure 4: Analysis for aluminum-graphene composite structure.The running time-average of N_t^2 illustrating convergence.(b) Temperature dependent $\langle N^2 \rangle_t$ conductivity extrapolated from experimental conductivity at 300 K from Reference [44].

Mott-type picture, this trend indicates a semiconducting-like response at the Al–Gr interface where thermal fluctuations promote near-E_F states and enhance the time-averaged overlap between occupied and accessible electronic states.

This behavior contrasts with previous simulations of flat single- and double-layer Al–Gr composites, which report a metal-like decrease in $\sigma(T)$ with increasing temperature [36], although at fixed temperature the conductivity increases as the Al–C distance is reduced from 3.41 to 2.97 Å. The metallic-to-semiconducting behavior in the Al–Gr composite arises from its microstructure—aluminum coupled to a multilayer, undulating graphene stack—which appears to stabilize and thermally activate interfacial conduction channels, leading to the monotonic increase in conductivity. To our knowledge, this provides the first atomistic evidence of semiconducting behavior in multilayer (> 3-layer) Al–Gr composites with a worm-like graphene morphology, consistent with high-resolution imaging observations by Kappagantula *et al.* [46].
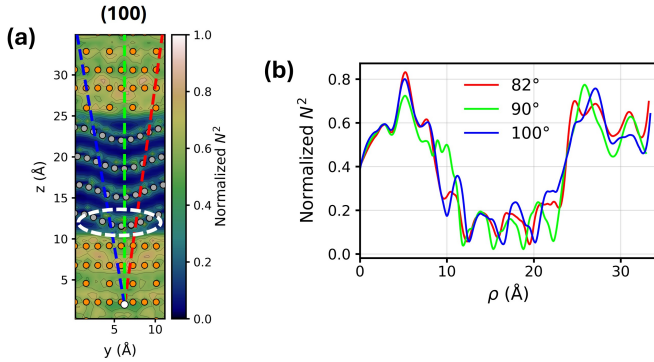

Figure 5: Spatial projection of N^2 electronic activity in the Al-graphene composite. (a) 2D colormap of normalized N^2 on a (100) plane slice at $x \approx 6.0$ Å. (b) Radial (ρ) profiles of N^2 extracted along the colored traces in (a) at the indicated projection angles θ.

The N^2 method [22] was employed to visualize conduction-active regions in the aluminum–graphene composite. Whereas TAHM captures the time-averaged near-E_f electronic activity along an MD trajectory, N^2 projects the near-E_f contributions into real space, revealing where conduction pathways form across heterogeneous regions. Figure 5a shows the (100)

cross-section at $x = 6$ Å. The dashed white oval marks the region where the lower carbon layer (gray spheres) is closest to the upper aluminum matrix (orange spheres), with a distance of ≈ 2.36 Å. The contour map (normalized N^2) spans 0 (blue) to 1 (white). The colored traces (green, red, and blue) are radial cuts taken along near-by in-plane directions (82°, 90° and 100°), showing how near-E_f activities varies with distance from the Al/C interface. The resulting peak-suppression-recovery pattern in Figure 5b reflects enhanced interfacial electronic activity, its attenuation into the amorphous graphene layers, and its re-emergence beyond the Al-C interaction zone.

3.3. Amorphous and Liquid Silicon

Figure 6a shows the temporal fluctuations of the mean Kohn-Sham eigenvalues of the states near the Fermi level at each temperature, serving as a direct probe of near-E_F electronic fluctuations induced by thermal lattice motion for temperatures from 200 to 1800 K. At low temperatures, the EDOS above and below E_F remain well separated, persisting the band-gap. With increasing temperature, particularly beyond 1200 K (and around its melting point of ≈ 1420 K [47]), pronounced broadening and overlap of these states are observed, signaling thermally driven delocalization of the electronic states near the band edges [24, 48, 49]. Figure S5a and b shows the instantaneous N_t^2 across the temperatures and its running time-average convergence.
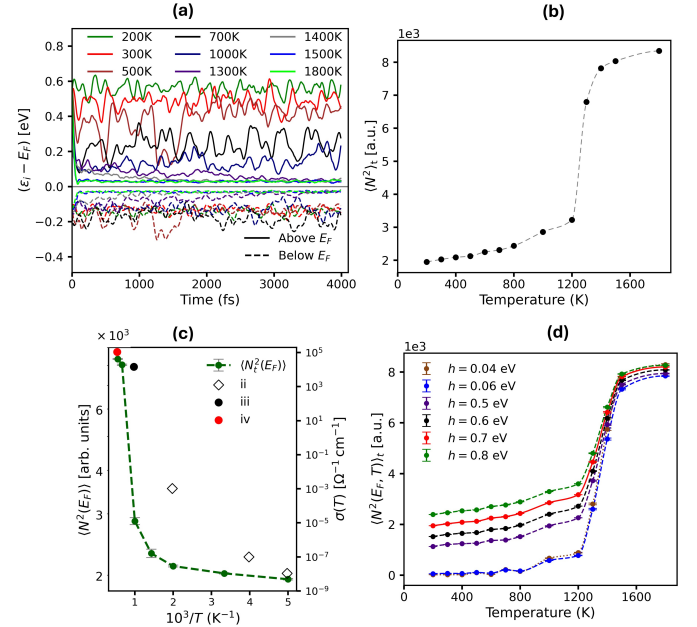

Figure 6: Analysis for amorphous silicon. (a) Thermal fluctuation of near-gap states ($E_f = 0$) at temperatures between 200 to 1800K. (b) Converged $\langle N^2 \rangle_t$ values as a function of temperature. (c) Comparison of $\langle N^2 \rangle_t$ with experimental data points from References (ii) [30], (iii) [31] and (iv) [32]. (d) Dependence of $\langle N^2 \rangle_t$ on the Gaussian broadening (h) used to obtain the instantaneous $N^2(E_f, T, t)$.

$\langle N^2 \rangle_t$ remains nearly constant up to about 1000 K and then increases sharply between 1200 and 1500 K (Figure 6b) . This

rapid rise, followed by a slight plateau, mirrors the experimentally observed behavior of the electrical conductivity of liquid silicon at high temperatures [50]. The trend reflects a phase transition as the system approaches its melting point (≈ 1420 K; Figure 2d). At these elevated temperatures, strong thermal atomic motion and dynamic structural arrangements in the disordered liquid network enhance the overlap among electronic states near the Fermi level, facilitating carrier hopping and improving electronic connectivity [24].

Figure 6c compares the trend of $\langle N^2 \rangle_t$ to experimentally measured conductivities [30, 31, 32]. Both show the characteristic exponential rise of conductivity with temperature expected for thermally activated transport in amorphous semiconductors, followed by a transition toward non-semiconducting behavior near the melting regime. The agreement between the computed and experimental trends indicates $\langle N^2 \rangle_t$ captures the essential physics of thermally assisted delocalization in a-Si [51, 52].

We also investigate the effects of different Gaussian broadening, h used to obtain $N^2(E_f, T, t)$ in Equation 5. As shown in Figure 6d, the overall trend remains consistent for different h values from 0.04 eV to 0.8 eV; with wider spread at temperatures below the jump at 1200 K, and more convergence at higher temperatures (> 1350 K).
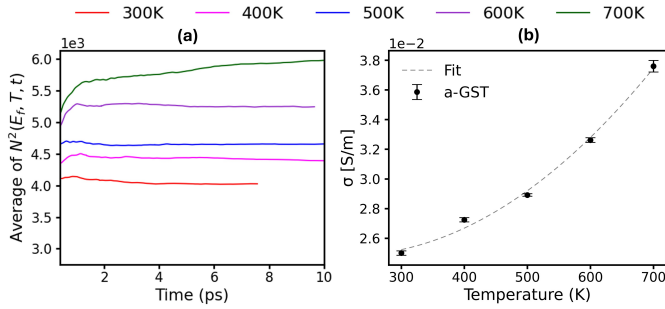

Figure 7: Analysis for amorphous Germanium–Antimony–Telluride. (a) The running time-average of N_t^2 illustrating convergence. (b) Temperature dependent $\langle N^2 \rangle_t$ conductivity extrapolated from experimental conductivity at 300 K from Reference [53].

3.4. Germanium–Antimony–Telluride

Similar to the Al–Gr composite, a-GST exhibits semiconducting behavior characterized by an increase in $\langle N^2 \rangle_t$ with temperature as shown by the convergence of the running time-average plot in Figure 7a for the temperature range of 300 – 700 K (See the instantaneous N_t^2 plot in Figure S6). This trend is consistent with the expected response of a-GST, where thermal excitation promotes carrier activation across its narrow mobility gap [54, 55]. The a-GST model employed in this study exhibits a band-gap of approximately 0.54 eV, with a mid-gap state located about 0.31 eV below the LUMO (See model "M5" in Reference [33]).

The conductivity of a-GST, shown in Figure 7b shows nearly linear increase with temperature. This is is consistent with experimental reports of thermally activated conductivity in a-GST [55, 53]. The $\langle N^2 \rangle_t$ fit to conductivity was carried out

using the experimentally measured average conductivity of a-GST at 300 K ($\sigma_{\exp} \approx 0.025$ S/m) [53] gives a proportionality constant of $\eta \approx 6.204 \times 10^{-6}$.

4. Conclusion

We have developed and demonstrated the TAHM method that extends Mott and Hindley's simplified picture of electronic transport into the time domain. By averaging the squared fluctuations of near-Fermi-level electronic density of states obtained along *ab initio* molecular dynamics trajectories, the method captures the coupling between lattice motion, electronic disorder, and charge transport. When scaled to a single experimental conductivity value, the resulting temperature-dependent trends reproduce the observed behavior across metallic, semiconducting, composite, and amorphous systems. The method predicts metallic reduction in conductivity as well as semiconducting increase with increasing temperature from TAHM.

For aluminum crystal and aluminum with a grain boundary, TAHM shows a monotonic decrease with increasing temperature, consistent with Bloch–Grüneisen electron–phonon scattering. In contrast, the multilayer, worm-like aluminum–graphene composite displays a semiconducting-like increase in TAHM with temperature, reflecting thermally activated interfacial conduction pathways stabilized by its microstructure. In amorphous silicon, TAHM remains nearly constant at low temperature but rises sharply between 1200 and 1500 K, coinciding with the onset of gap closure and the semiconductor-metal (melting) transition. The a-GST system exhibits a steady, nearly linear increase in TAHM with temperature, consistent with thermally activated carrier excitation across a mobility gap.

Together, these results establish the TAHM method as a simple yet predictive microscopic descriptor of temperature-dependent electronic transport that is transferable across diverse structural and electronic regimes. The framework provides a computationally efficient and physically transparent complement to other Kubo–Greenwood-based formulations, enabling rapid assessment of conductivity trends in nanostructured, composite, and disordered materials.

References

[1] J. M. Ziman, Formal transport theory, in: Electrons and Phonons: The Theory of Transport Phenomena in Solids, Oxford University Press, 2001, Ch. 7. doi:10.1093/acprof:oso/9780198507796.003.0007.

[2] F. Giustino, Electron-phonon interactions from first principles, Rev. Mod. Phys. 89 (2017) 015003. doi:10.1103/RevModPhys.89.015003.

[3] G. S. Rocha, M. N. Ferreira, G. S. Denicol, J. Noronha, Transport co-efficients of quasiparticle models within a new relaxation time approximation of the boltzmann equation, Phys. Rev. D 106 (2022) 036022. doi:10.1103/PhysRevD.106.036022.

[4] R. Claes, S. Poncé, G.-M. Rignanese, G. Hautier, Phonon-limited electronic transport through first principles, Nature Reviews Physics 7 (2) (2025) 73–90. doi:10.1038/s42254-024-00795-0.

[5] G. K. Madsen, D. J. Singh, Boltztrap. a code for calculating band-structure dependent quantities, Computer Physics Communications 175 (1) (2006) 67–71. doi:10.1016/j.cpc.2006.03.007.

[6] G. K. Madsen, J. Carrete, M. J. Verstraete, Boltztrap2, a program for interpolating band structures and calculating semi-classical transport coefficients, Computer Physics Communications 231 (2018) 140–145. doi:10.1016/j.cpc.2018.05.010.

[7] S. Poncé, E. Margine, C. Verdi, F. Giustino, Epw: Electron–phonon coupling, transport and superconducting properties using maximally localized wannier functions, Computer Physics Communications 209 (2016) 116–133. doi:10.1016/j.cpc.2016.07.028.

[8] C. Ringhofer, Numerical methods for the semiconductor boltzmann equation based on spherical harmonics expansions and entropy discretizations, Transport Theory and Statistical Physics 31 (4-6) (2002) 431–452. doi:10.1081/TT-120015508.

[9] R. Kubo, M. Yokota, S. Nakajima, Statistical-mechanical theory of irreversible processes. ii. response to thermal disturbance, Journal of the Physical Society of Japan 12 (11) (1957) 1203–1211.

[10] M. S. Green, Markoff random processes and the statistical mechanics of time-dependent phenomena. ii. irreversible processes in fluids, The Journal of Chemical Physics 22 (3) (1954) 398–413. doi:10.1063/1.1740082.

[11] M. S. Green, Markoff random processes and the statistical mechanics of time-dependent phenomena, The Journal of Chemical Physics 20 (8) (1952) 1281–1295. doi:10.1063/1.1700722.

[12] R. Kubo, M. Toda, N. Hashitsume, Statistical Physics II: Nonequilibrium Statistical Mechanics, Solid-State Sciences, Springer Berlin, Heidelberg, 1985. doi:10.1007/978-3-642-58244-8.

[13] D. A. Greenwood, The Boltzmann equation in the theory of electrical conduction in metals, Poceedings of the Physical Society of London 71 (460) (1958) 585–596. doi:10.1088/0370-1328/71/4/306.

[14] S. K. Bose, O. Jepsen, O. K. Andersen, Real-space calculation of the electrical resistivity of liquid 3d transition metals using tight-binding linear muffin-tin orbitals, Phys. Rev. B 48 (1993) 4265–4275. doi:10.1103/PhysRevB.48.4265. URL https://link.aps.org/doi/10.1103/PhysRevB.48.4265

[15] L. Calderín, V. Karasiev, S. Trickey, Kubo–Greenwood electrical conductivity formulation and implementation for projector augmented wave datasets, Computer Physics Communications 221 (2017) 118–142. doi:10.1016/j.cpc.2017.08.008.

[16] J. Dufty, J. Wrighton, K. Luo, S. Trickey, On the kubo-greenwood model for electron conductivity, Contributions to Plasma Physics 58 (2-3) (2018) 150–154. doi:10.1002/ctpp.201700102.

[17] K. Prasai, K. N. Subedi, K. Ferris, P. Biswas, D. A. Drabold, Spatial projection of electronic conductivity: The example of conducting bridge memory materials, physica status solidi (RRL) – Rapid Research Letters 12 (9) (2018) 1800238. doi:10.1002/pssr.201800238.

[18] K. N. Subedi, K. Prasai, D. A. Drabold, Space-projected conductivity and spectral properties of the conduction matrix, physica status solidi (b) 258 (2021) 2000438. doi:10.1002/pssb.202000438.

[19] N. Mott, Conduction in glasses containing transition metal ions, Journal of Non-Crystalline Solids 1 (1) (1968) 1–17. doi:https://doi.org/10.1016/0022-3093(68)90002-1. URL https://www.sciencedirect.com/science/article/pii/0022309368900021

[20] N. F. Mott, E. A. Davis, Theory of electrons in a non-crystalline medium, in: Electronic Processes in Non-crystalline Materials, 2nd Edition, Clarendon/Oxford University Press, Oxford, New York, 1979, Ch. 2, pp. 11–15.

[21] N. K. Hindley, Random phase model of amorphous semiconductors ii. hot electrons, Journal of Non-Crystalline Solids 5 (1) (1970) 31–40. doi:10.1016/0022-3093(70)90194-8.

[22] K. Nepal, C. Ugwumadu, F. Kraft, Y. Al-Majali, D. Drabold, The effects of crystal orientation and common coal impurities on electronic conductivity in copper–carbon composites, Carbon 231 (2025) 119711. doi:10.1016/j.carbon.2024.119711.

[23] C. Ugwumadu, D. A. Drabold, R. M. Tutchton, Effects of galactic irradiation on thermal and electronic transport in tungsten, physica status solidi (b) 262 (11) (2025) 2500109. doi:10.1002/pssb.202500109.

[24] T. A. Abtew, M. Zhang, D. A. Drabold, Ab initio estimate of temperature dependence of electrical conductivity in a model amorphous material: Hydrogenated amorphous silicon, Phys. Rev. B 76 (2007) 045212. doi:10.1103/PhysRevB.76.045212.

[25] K. N. Subedi, K. Kappagantula, F. Kraft, A. Nittala, D. A. Drabold, Electrical conduction processes in aluminum: Defects and phonons, Phys. Rev. B 105 (2022) 104114. doi:10.1103/PhysRevB.105.104114.

[26] A. Chowdhury, S. Bhattacharjee, Experimental investigation of change in sheet resistance and debye temperatures in metallic thin films due to low-energy ion beam irradiation, Journal of Physics D: Applied Physics 46 (43) (2013) 435304.

[27] R. Thapa, C. Ugwumadu, K. Nepal, J. Trembly, D. A. Drabold, Ab initio simulation of amorphous graphite, Phys. Rev. Lett. 128 (2022) 236402. doi:10.1103/PhysRevLett.128.236402.

[28] C. Ugwumadu, R. Thapa, K. Nepal, D. A. Drabold, Atomistic nature of amorphous graphite, European Journal of Glass Science and Technology Part B 64 (2023) 16–22. doi:10.13036/17533562.64.1.18.

[29] K. Nepal, C. Ugwumadu, A. Gautam, K. Kappagantula, D. A. Drabold, Electronic conductivity in metal-graphene composites: the role of disordered carbon structures, defects, and impurities, Journal of Physics: Materials 7 (2) (2024) 025003. doi:10.1088/2515-7639/ad261a.

[30] A. Lewis, Evidence for the mott model of hopping conduction in the anneal stable state of amorphous silicon, Phys. Rev. Lett. 29 (1972) 1555–1558. doi:10.1103/PhysRevLett.29.1555.

[31] S. S. Ashwin, U. V. Waghmare, S. Sastry, Metal-to-semimetal transition in supercooled liquid silicon, Phys. Rev. Lett. 92 (2004) 175701. doi:10.1103/PhysRevLett.92.175701.

[32] V. Glazov, S. Chizhevskaya, N. Glagoleva, Liquid Semiconductors, Monographs in semiconductor physics, Plenum Press, 1969.

[33] K. Nepal, A. Gautam, R. Hussein, K. Konstantinou, S. Elliott, C. Ugwumadu, D. Drabold, Electronic and thermal properties of the phase-change memory material, ge2sb2te5, and results from spatially resolved transport calculations, Solid State Sciences 173 (2026) 108182. doi:https://doi.org/10.1016/j.solidstatesciences.2025.108182.

[34] G. Kresse, J. Furthmüller, Efficient iterative schemes for ab initio total-energy calculations using a plane-wave basis set, Phys. Rev. B 54 (1996) 11169–11186. doi:10.1103/PhysRevB.54.11169.

[35] A. Nittala, J. Smith, B. Gwalani, J. Silverstein, F. F. Kraft, K. Kappagantula, Simultaneously improved electrical and mechanical performance of hot-extruded bulk scale aluminum-graphene wires, Materials Science and Engineering: B 293 (2023) 116452. doi:10.1016/j.mseb.2023.

116452.

[36] K. Nepal, C. Ugwumadu, K. N. Subedi, K. Kappagantula, D. A. Drabold, Physical origin of enhanced electrical conduction in aluminum-graphene composites, Applied Physics Letters 124 (9) (2024) 091902. doi:10.1063/5.0195967.

[37] B. R. Djordjević, M. F. Thorpe, F. Wooten, Computer model of tetrahedral amorphous diamond, Phys. Rev. B 52 (1995) 5685–5689. doi:10.1103/PhysRevB.52.5685.

[38] F. Wooten, K. Winer, D. Weaire, Computer generation of structural models of amorphous si and ge, Phys. Rev. Lett. 54 (1985) 1392–1395. doi:10.1103/PhysRevLett.54.1392.

[39] D. Igram, B. Bhattarai, P. Biswas, D. Drabold, Large and realistic models of amorphous silicon, Journal of Non-Crystalline Solids 492 (2018) 27–32. doi:10.1016/j.jnoncrysol.2018.04.011.

[40] C. Ugwumadu, A. Gautam, Y. G. Lee, D. A. Drabold, Mapping thermal conductivity at the atomic scale: A step toward the thermal design of materials, physica status solidi (b) 2500316doi:10.1002/pssb.202500316.

[41] P. E. Blöchl, Projector augmented-wave method, Phys. Rev. B 50 (1994) 17953–17979. doi:10.1103/PhysRevB.50.17953.

[42] J. P. Perdew, K. Burke, M. Ernzerhof, Generalized gradient approximation made simple, Phys. Rev. Lett. 77 (1996) 3865–3868. doi:10.1103/PhysRevLett.77.3865.

[43] S. Nosé, A unified formulation of the constant temperature molecular dynamics methods, The Journal of Chemical Physics 81 (1) (1984) 511–519. doi:10.1063/1.447334.

[44] B. Smyrak, M. Gniełczyk, Study of the effect of graphene content on the electrical and mechanical properties of aluminium–graphene composites, Materials 18 (2025) 590. doi:10.3390/ma18030590.

[45] N. Ashcroft, N. Mermin, Solid State Physics, Holt, Rinehart and Winston, 1976.

[46] K. S. Kappagantula, Reza-E-Rabby, A. M. Nittala, H. Das, J. Christudasjustus, T. Poudel, S. Wolff, Bulk-scale ultra-conductors via low-c manufacturing pathways, Tech. rep., DOE Vehicles Technology Office Annual Merit Review (2025).
URL https://www1.eere.energy.gov/vehiclesandfuels/downloads/2025_AMR/MAT294_Kappagantula_2025_o.pdf

[47] E. P. Donovan, F. Spaepen, D. Turnbull, J. M. Poate, D. C. Jacobson, Heat of crystallization and melting point of amorphous silicon, Applied Physics Letters 42 (8) (1983) 698–700. doi:10.1063/1.94077.

[48] D. A. Drabold, P. A. Fedders, S. Klemm, O. F. Sankey, Finite-temperature properties of amorphous silicon, Phys. Rev. Lett. 67 (1991) 2179–2182. doi:10.1103/PhysRevLett.67.2179.

[49] J. Li, D. Drabold, Electron hopping between localized states: A simulation of the finite-temperature anderson problem using density functional methods, Physical Review B 68 (3) (2003) 033103.

[50] H. Sasaki, A. Ikari, K. Terashima, S. K. Shigeyuki Kimura, Temperature dependence of the electrical resistivity of molten silicon, Japanese Journal of Applied Physics 34 (7R) (1995) 3426. doi:10.1143/JJAP.34.3426.

[51] J. Li, D. Drabold, Atomistic simulation of the finite-temperature anderson localization problem, physica status solidi (b) 233 (1) (2002) 10–17. doi:10.1002/1521-3951(200209)233:1<10::AID-PSSB10>3.0.CO;2-V.

[52] J. Li, D. A. Drabold, Electron hopping between localized states: A simulation of the finite-temperature anderson problem using density functional methods, Phys. Rev. B 68 (2003) 033103. doi:10.1103/PhysRevB.68.033103.

[53] T. Kato, K. Tanaka, Electronic properties of amorphous and crystalline ge2sb2te5 films, Japanese Journal of Applied Physics 44 (10R) (2005) 7340. doi:10.1143/JJAP.44.7340.

[54] B.-S. Lee, J. R. Abelson, S. G. Bishop, D.-H. Kang, B.-k. Cheong, K.-B. Kim, Investigation of the optical and electronic properties of ge2sb2te5 phase change material in its amorphous, cubic, and hexagonal phases, Journal of Applied Physics 97 (9) (2005) 093509. doi:10.1063/1.1884248.

[55] S. Muneer, J. Scoggin, F. Dirisaglik, L. Adnane, A. Cywar, G. Bakan, K. Cil, C. Lam, H. Silva, A. Gokirmak, Activation energy of metastable amorphous ge2sb2te5 from room temperature to melt, AIP Advances 8 (6) (2018) 065314. doi:10.1063/1.5035085.